



This is a repository copy of *A global environmental crisis 42,000 years ago*.

White Rose Research Online URL for this paper:
<https://eprints.whiterose.ac.uk/188230/>

Version: Supplemental Material

Article:

Cooper, A., Turney, C.S.M., Palmer, J. et al. (30 more authors) (2021) A global environmental crisis 42,000 years ago. *Science*, 371 (6531). pp. 811-818. ISSN 0036-8075

<https://doi.org/10.1126/science.abb8677>

This is the author's version of the work. It is posted here by permission of the AAAS for personal use, not for redistribution. The definitive version was published in *Science* on Vol 371, Issue 6531, 19 Feb 2021, DOI: <https://doi.org/10.1126/science.abb8677>

Reuse

Items deposited in White Rose Research Online are protected by copyright, with all rights reserved unless indicated otherwise. They may be downloaded and/or printed for private study, or other acts as permitted by national copyright laws. The publisher or other rights holders may allow further reproduction and re-use of the full text version. This is indicated by the licence information on the White Rose Research Online record for the item.

Takedown

If you consider content in White Rose Research Online to be in breach of UK law, please notify us by emailing eprints@whiterose.ac.uk including the URL of the record and the reason for the withdrawal request.



eprints@whiterose.ac.uk
<https://eprints.whiterose.ac.uk/>

Materials and Methods for *A Global Environmental Crisis 42,000 Years Ago* by Cooper *et al.*

Ancient kauri (*Agathis australis*) from Northland, New Zealand

Four swamp-preserved kauri trees associated with the Laschamps Excursion (hereafter Laschamps) were obtained from Ngāwhā Springs (Nga001; site location: -35.402707°, 173.858597°), Kai Iwi Lakes (FIN09 and FIN14058; site location: -35.810426°, 173.630594°) and Mangawhai (NZKL1855; site location: -36.142502°, 174.609489°) in northern New Zealand (Fig. S1). Nga001 came from a power plant development site in the central part of Northland and appears to have been encased by sediments associated with geothermal activity (Fig. S2); the first time that we are aware of a kauri log being found encased in geothermal deposits of any kind. FIN09 and FIN14058 are cross-sections from logs that were extracted on two (nearly) adjacent farms, along the west coast of Northland that are owned by the Finlayson family. These two sites are positioned within a late Pleistocene parabolic dune belt that contains pockets of wood-rich peat deposits. NZKL1855 is a section of a swamp kauri table top that was obtained from New Zealand Kauri LTD after the primary log had been milled; this sample is believed to originate from Black Swamp Road, Mangawhai, which is positioned within a Northland east coast MIS5 relic foredune ridge sequence facing the Pacific Ocean and containing abundant Marine Isotope Stage 3 peat and wood (1).

Multiple cross-sections (or ‘biscuits’) were cut from Nga001, FIN09, FIN14058, and radial strips were removed for measurement while the residual offcuts were archived (Fig. S3). Only one set of radial sections were obtained from NZKL1855 because it was a tabletop panel pre-cut from the center of a tree trunk. When NZKL1855 was cut in the mill yard, pith was visibly offset from the center of the table, creating two radii of unequal lengths consistent with asymmetric growth of that tree (common for kauri). All of the radial strips were dried and then sanded progressively from coarse to fine grit paper until a highly polished surface was obtained. The finished radii were studied under a binocular microscope and the annual rings identified and counted. Following this step, rings were measured using standard dendrochronology techniques employing a travelling stage with an incorporated digital linear encoder.

The four subfossil-kauri tree-ring series associated with the Laschamps Excursion did not indicate any immediate matching patterns of growth (i.e. cross matching). The absence of dendrochronological cross matching could be due to multiple factors, including, idiosyncratic issues related to individual trees (e.g. NZKL1855 is visibly damaged and suppressed towards the bark edge), the type of sample (FIN14058 is likely a branch, despite being nearly one meter in diameter), or attempting comparisons between a juvenile growth period (i.e. Nga001) with senescent tree phases (i.e. FIN14058, FIN09, NZKL1855). All are known issues that can hamper linking kauri tree-ring sequences, especially when sample numbers are limited. As such, the internal ring sequence count is considered robust for each of these trees, but there is currently no dendrochronological “lock” between the four samples (and their associated sequential ¹⁴C dates). Future work may help to refine this issue if sufficient

coeval samples are found, and all of our measurements have been archived for future cross-dating exercises (NOAA-ITRDB).

Comparisons of the average radial growth rates (mm/year) were made between the four ancient kauri trees as well as to modern kauri tree-ring collections and other subfossil samples from OIS3 (Fig. S4). The results clearly show that the Ngawha tree was noticeably slower growing than those growing slightly earlier (i.e. Fin14058, Fin09, NZKL1855) with the latter group being more consistent with modern trees and other samples from OIS3. Furthermore, the actual ring-width sequence (shown in Fig. 1c) shows a sustained decline in growth that coincides with the Adams Event and into the Laschamps. There is a natural tendency for radial ring widths to decline slowly over the life of a tree - commonly described as the age-related growth trend, however the Ngawha tree shows an abnormally slow growth pattern indicating unfavorable growing conditions.

The internal ring sequence mark-up for each radial sample was extended onto adjacent offcuts to enable destructive sampling for radiocarbon dating. Four-decade block samples were marked on each of the radii where feasible, with slight variation in some cases where ring width suppression hampered obtaining sufficient weight for high precision liquid scintillation spectroscopy (starting dry wood weights between 70-80g are required to produce 7.5ml benzene aliquots). Each multi-decadal sample was removed from either the radii or an offcut via careful chiseling along annual boundaries. As such, the internal age incorporation for most samples are 40 years. Chronological error due to missing rings for each tree is estimated to be <1% and would be isolated within millennial scale ring-sequences for each tree (2, 3). Across the multi-millennial sequential radiocarbon data set that has been developed in this study, the issue of missing rings is not considered a significant element that would contribute to compression or drift of the internal tree ring time scales and the spacing of adjacent ^{14}C blocks through time (2-4).

Sedimentary Sequences

Pillar Rock, subantarctic Auckland Islands: Located in the Pacific Sector of the Southern Ocean, the New Zealand subantarctic Auckland Islands (50°S, 166°E; Figs S1 and S5) are the eroded remnant of extensive Oligocene to Miocene basaltic volcanism (5), with rugged topography, reaching up to 664 m.a.s.l. The islands lie in the southwest Pacific in the core of Southern Hemisphere westerly winds and experience the same climate regime with relatively mild mean annual temperatures (6). Situated today between the Subtropical Front (approximately 45° S) and the cool Antarctic waters of the Antarctic Convergence (around 55° S), these ocean fronts may have shifted by up to 5° further northwards during the LGM (7) leading to a mean annual air temperature depression over the islands of ~6°C (8). The Auckland Islands are therefore highly sensitive to regional climate change during the late Pleistocene (8-10).

The exposed sedimentary sequence on a north-facing cliff near Pillar Rock, Auckland Island (-50.518°, 166.217°; 30 m.a.s.l.; Fig. S6), consists of glacial till overlain by a sequence of organic and non-organic units, providing important constraints on late Pleistocene environmental change in this sector of the Southern Ocean. The exposed section consists of a laterally continuous (~10 m), horizontally bedded section exposed by extensive cliff erosion along the north coast of Auckland Island at ~30 m.a.s.l. In places the section is over 4 m thick, and rests on several meters of deeply indurated diamicton, that we correlate with the upper till exposed on nearby

Enderby Island (10). The ‘Enderby Till’ at Pillar Rock is overlain non-conformably by stratified sands and gravels, which are iron banded. This unit is overlain by a ~2 m thick conformable sedimentary succession, that grades upwards from massive silts and sands into laminated silts and clays and into an organic-rich silt band. Above this organic silt the succession continues, with a conformable, non-erosive boundary into sandy silts, which become increasingly clast rich and less dense. This conformable sequence is topped by a 10 cm thick clast-supported gravel, topped by a 2 cm layer of flat lying gravel/pebbles. This succession is overlain unconformably by a 27 cm thick sequence of early Holocene humified dark brown peat. Above the peat, there is a series of horizontally bedded silty sandy loams and low organic soil horizons, with pebble horizons, overlain by ~20 cm of sandy loam at the surface. The organic units at Pillar Rock were sampled with monolith tins. Sediments were described in the field, with samples wrapped and transported back to the laboratory where they were cold-stored (4°C) prior to detailed pollen analysis and detailed radiocarbon dating.

A 26 cm long rectangular sedimentary section was dug out of Pillar Rock, capturing an 8 cm layer of highly compressed lignitic peat with sharp boundaries (Fig. S7), sitting on organic rich silts with weathered boulders, and overlain by grey-brown sandy silt with abundant stones. The lignite layer thus represents a stable interval in a prolonged period of periglacial activity. The entire lignite layer was sampled for pollen at 5 mm thick contiguous intervals (1.25 mm per sample). Samples for radiocarbon dating were taken from the top and bottom of the lignite, as 5 mm thick samples at the sharp boundaries, and contiguously down the profile at the same depths as the pollen samples. Pollen preparation followed standard techniques (11). Pollen was counted under x400 magnification until a sum of 250 grains were reached (excluding fern spores) and pollen expressed as a percentage of this sum.

Lake Towuti, Sulawesi: Lake Towuti is located at 2.5°S, 121.5°E on the island of Sulawesi in central Indonesia within the Indo-Pacific Warm Pool (IPWP) (12) (Fig. S9). The site lies at the center of the humid, unstable air mass overlying the IPWP, and its climate responds strongly to large-scale changes in regional atmospheric circulation and sea surface temperature associated with the Australian–Indonesian summer monsoon (AISM). The Lake Towuti basin receives ~2,700 mm of precipitation annually and is surrounded by dense closed-canopy rainforest (13). Today, this region experiences a wet season from December to May when the Intertropical Convergence Zone (ITCZ) migrates southward over the region (14).

Lake Towuti is the largest tectonic lake in Indonesia, and at 205 m depth, its sediments preserve perhaps the longest and most continuous terrestrial record of climate available from the region. In 2007–2010, 13 sediment piston cores were recovered from Lake Towuti (12). Here we focus on the most continuous radiocarbon-dated stratigraphy from core TOW10- 9B (Fig. S10). As part of a comprehensive multi-proxy study, carbon-isotopic composition of long-chain, even-numbered n-alkanoic acids ($\delta^{13}\text{C}_{\text{wax}}$) was measured, a main component of plant epicuticular waxes. The $\delta^{13}\text{C}_{\text{wax}}$ is primarily used to distinguish between plants using C_3 and C_4 photosynthetic pathways (15) because C_4 plants use a CO_2 -concentrating mechanism that improves their photorespiration and water-use efficiency relative to C_3 plants (16). Precipitation is the dominant control on the distribution of C_3 and C_4 plants through much of the tropics, such that $\delta^{13}\text{C}_{\text{wax}}$ has been widely used to reconstruct past changes in tropical hydroclimate (12, 17, 18). Global surveys of the $\delta^{13}\text{C}$ of vegetation indicate these processes can cause ~6‰ depletion in the $\delta^{13}\text{C}$ of leaf matter in tropical rainforests relative to more xeric C_3 ecosystems, and ~4‰

depletion in tropical rainforests relative to drier, tropical deciduous forests (19, 20). Thus, we interpret more depleted $\delta^{13}\text{C}_{\text{wax}}$ to represent C_3 forests growing in wet conditions; whereas, enriched $\delta^{13}\text{C}_{\text{wax}}$ reflects a drier climate and increasing C_4 grasses (12).

Previous work has reported the $\delta^{13}\text{C}_{\text{wax}}$ values. To summarize, lipid extraction, purification, and isotopic analysis followed the procedures outlined in ref. (12). Between 2 and 10 g of freeze-dried, powdered sediment samples were extracted using a Dionex 350 accelerated solvent extractor with a 9:1 solution of CH_2Cl_2 :MeOH. Acid fractions of lipid extracts were separated from neutral and polar fractions using aminopropyl silica gel column chromatography with 2:1 CH_2Cl_2 :isopropanol and 4% acetic acid in anhydrous ethyl ether as eluents. The acid fraction was methylated using acetyl chloride in methanol of a known isotopic composition to allow isotopic correction of fatty acid methyl esters (FAMES). FAMES were further purified using silica gel columns with hexane and CH_2Cl_2 as eluents. The CH_2Cl_2 fraction containing saturated FAMES was dried under N_2 gas and then dissolved in toluene before isotopic analysis. Carbon isotopes of the leaf waxes ($\delta^{13}\text{C}_{\text{wax}}$) were run in duplicate or more on a Thermo Finnegan Delta XL gas chromatograph isotope ratio mass spectrometer at Brown University and are reported relative to Vienna Pee Dee Belemnite. All $\delta^{13}\text{C}_{\text{wax}}$ data are corrected for the isotopic composition of the methyl group added during methylation. 145 samples were analyzed for the $\delta^{13}\text{C}$ of C_{28} n-acid, the most abundant homolog in our samples (Fig. S11). 119 and 58 samples had sufficient abundances to measure the $\delta^{13}\text{C}$ of C_{26} and C_{30} n-acid, respectively. The average difference between duplicated samples in the $\delta^{13}\text{C}$ of C_{28} n-acid is 0.17‰, and the pooled SE of samples ($n = 20$) measured in triplicate or greater is 0.47‰.

As part of this study, the core TOW10-9B was also subjected to measurements of natural remnant magnetization (NRM) as well as $\text{NRM}_{20\text{mT}}$, which is the NRM after alternating field (AF) demagnetization to a peak field of 20 mT (21). Here, the AF demagnetization was demonstrably effective in isolating the secondary NRM carried by large multidomain (MD) grains, which have a coercivity ≤ 20 mT (22). The core was also subjected to measurements of $\text{ARM}_{20\text{mT}}$ and $\text{IRM}_{20\text{mT}}$, which are the intensities of ARM and SIRM after an AF demagnetization to a peak field of 20 mT, respectively. The ARM susceptibility, denoted by κ_{ARM} , was calculated by dividing the measured ARM with the value of a superimposed steady magnetic field of 0.05 mT (23). The measurements of $\text{NRM}_{20\text{mT}}$, $\text{ARM}_{20\text{mT}}$ and $\text{IRM}_{20\text{mT}}$ were carried out in the Paleomagnetic Laboratory of the University of Rhode Island using a 2G-Enterprises cryogenic magnetometer with a measurement interval of 1 cm (Fig. S11). In the Lake Towuti sediments which contain high concentrations of MD grains, the paleointensity values were calculated by normalizing the $\text{NRM}_{20\text{mT}}$ values with respect to other magnetic parameters in order to isolate the effects of the geomagnetic field.

Radiocarbon Dating and Calibration

Here we report radiocarbon (^{14}C) ages as thousands of years Before Present (CE 1950) i.e. ka ^{14}C BP, with calibrated ^{14}C and calendar ages given as thousands of calendar years (ka) Before Present.

Ancient kauri (Agathis australis): For radiocarbon dating the ancient kauri, chemical pretreatment of the four decadal-long wood samples was carried out to extract alpha-cellulose – the wood fraction deemed the most reliable for minimizing potential contamination – and measured using High-Precision Liquid Scintillation Counting (HP-LSC) at the University of Waikato, in order to provide the most robust ^{14}C ages which are required for such high-precision

study (Table S1) (24). Wood pretreatment protocols followed those outlined in Hogg *et al.* (25). Seventy-gram samples were ground to pass a 20-mesh sieve. Soxhlet apparatus was used to extract resins utilizing acetone for 6 hr followed by distilled water for 6 hr. Holocellulose was produced by repeated bleaching in acidified NaClO₂ (15 g/L). The alpha-cellulose fraction (~40% of initial wood weight) was obtained by a final extraction in 5% NaOH (under N₂ gas), followed by acidification in 5% HCl and washing in distilled water. Radiocarbon ages were determined by decay counting in Perkin Elmer Wallac QuantulusTM spectrometers. Cellulose samples were converted to benzene in vacuum systems preconditioned for activities of approximately seven half-lives, utilizing 7.5 g benzene samples contained within 'Waikato' synthetic silica counting vials (26) and measured for a minimum of 10,000 minutes per sample. The Modern and Background standards (OXII and Oxygen Isotope Stage-5 Renton Road sub-fossil kauri wood respectively) were prepared and measured in a similar manner. Background blank activity derived from repeat (13 measurements) over a two-year period of the Renton Road kauri alpha-cellulose was equivalent to 0.00041 ± 0.00009 times Modern (~62.7 kyr BP), with the Background blank uncertainty obtained from the gaussian standard deviation of all measurements. Isotopic fractionation correction was achieved by measuring $\delta^{13}\text{C}$ for all samples using a Europa Scientific Penta 20/20 isotope ratio spectrometer.

Calibration Curve: A ¹⁴C kauri-Hulu Southern Hemisphere (SH) calibration curve was constructed to cover 30-50 ka (Figs. S12 and S13). The sub-fossil kauri ¹⁴C determinations were combined with the 249 ¹⁴C determinations from the two ²³⁰Th-dated Hulu Cave speleothems (MSD and MSL) (27) during this time period. Curve construction was performed using the same Bayesian spline with errors-in-variables statistical approach used for the IntCal20 and SHCal20 curves (28-30). Non-informative priors were placed on the absolute calendar ages of the oldest ¹⁴C determination of each floating kauri tree-ring sequence. The robust, internal, ring sequence counts then provided relative and known age increments with respect to these oldest calendar ages. Within the Markov Chain Monte Carlo (MCMC) fitting procedure, in addition to calibration curve construction, posterior absolute calendar ages for each floating tree-ring sequence were simultaneously estimated based upon fit with both the Hulu data and the other kauri.

The Hulu cave speleothem data were modelled to have an offset r_i , measured in radiocarbon years, to the atmospheric SH kauri due to the dead carbon fraction (DCF) present in the Hulu speleothems and the North-South (NS) interhemispheric radiocarbon offset. The offset for any Hulu determination was considered as independent and identically distributed $r_i \sim N(\nu, \zeta^2)$ i.e. additional independent variation around a constant, unknown mean. Here ν represents the unknown mean kauri-Hulu offset and ζ the level of independent variation around the mean. A prior was placed on the mean kauri-Hulu offset of $\pi(\nu) \sim N(480 - 36 = 444, 100^2)$ based upon the 480 ¹⁴C yr mean DCF offset seen between the H82 Hulu cave speleothem (31) and the Northern Hemisphere tree ring determinations of IntCal20 (28); with the 36 ¹⁴C yr mean NS radiocarbon offset of SHCal20 subtracted (30). Since these initial offset estimates were based upon the 0-14 ka time period, as opposed to 30-50 ka, a difference in mean of ± 100 ¹⁴C yr (1σ) for our period of interest was considered prudent. The nature of speleothems means that the radiocarbon signal recorded in the Hulu Cave is also believed to be somewhat smoothed, so that atmospheric radiocarbon fluctuations on short timescales are effectively lost (32). The independent uncertainty ζ around the mean offset aims to account for this along with both

potential annual variation in the Hulu DCF and the NS radiocarbon offset. The Hulu H82 speleothem is seen to require an additional uncertainty of ~ 50 ^{14}C yr for consistency with atmospheric tree ring determinations (29), while the NS offset in SHCal20 has an uncertainty of ~ 27 ^{14}C yr (30). Adding in quadrature provided an estimate for ζ , the additional independent uncertainty in the kauri-Hulu offset for any determination, of 57 ^{14}C yr.

The Bayesian spline used to model the calibration curve was constructed using 150 knots to permit potential fine scale detail in the resultant curve to be captured while still enabling practical estimation. In the 40-45 ka period that covered the potential fitting locations of the floating kauri trees, 103 evenly spaced knots were used in order to penalize all possible calendar age placements of the kauri equitably (Table S1). Outside this range, knots were placed at quantiles of the observed Hulu data. A non-informative prior was placed on the level of smoothing. The MCMC was run for 250,000 iterations. The first 125,000 of these iterations were discarded as burn-in. The remaining 125,000 were used to create the final calibration curve. This curve is shown in Figs. S12 (in $\Delta^{14}\text{C}$) and S13 (in radiocarbon age), and the posterior calendar age estimate of each kauri in Fig. S14. Further, 500 individual calibration curve realizations from the posterior (each representing a plausible historical record of SH atmospheric radiocarbon) were extracted for use in synchronizing our radiocarbon and ice core chronologies.

For ~ 800 years prior to the prominent $\Delta^{14}\text{C}$ increase captured in our composite radiocarbon record, we also observe a quasi-centennial oscillatory data structure that tapers from high to low amplitude that is followed by a punctuated radiocarbon enrichment starting at ~ 43 ka (30). We consider this pattern in the radiocarbon data to be sound because of the demonstrable reproducibility in the ^{14}C measurements, and similarity to previously published records (27, 33). This pattern is also independently replicated in different ways via similar characteristics seen in ^{10}Be variations captured in ice cores (Fig. 1) (34). The ^{14}C centennial-scale pattern prior to the Adams Event is comparable to the Holocene 207-year de Vries solar cycle pattern that has also been observed in the Greenland ice core ^{10}Be data around Laschamps (35), so may represent low-frequency solar variability. The levels of atmospheric radiocarbon remain elevated after the Laschamps for >1000 years as has been observed previously, most likely a consequence of global carbon cycle changes, including Heinrich Event 4 (27).

Peat and lake sediments: The contiguous peat and lake sediments analyzed here were given an acid-base-acid (ABA) pretreatment. Because of the relatively small amount of material available (compared to the kauri), samples were measured by accelerator mass-spectrometry (AMS). Here the pretreated peat and lake sediments were combusted and graphitized in the University of Waikato AMS laboratory, with $^{14}\text{C}/^{12}\text{C}$ measurement by the University of California at Irvine (UCI) on a NEC compact (1.5SDH) AMS system. The pretreated samples were converted to CO_2 by combustion in sealed pre-baked quartz tubes, containing Cu and Ag wire. The CO_2 was then converted to graphite using H_2 and a Fe catalyst, and loaded into aluminium target holders for measurement at UCI. To generate an age model for the sequences, we used the new combined kauri-Hulu Cave calibration dataset generated here (see above) using a *P_sequence* deposition model with the General Outlier analysis option (with probability value of 0.05) in OxCal 4.2 (ref. (36, 37)) (Tables S2 and S3). For Pillar Rock and Lake Towuti, previously ages reported by ref. (10) and ref. (12) respectively were integrated in the age models (Figs S6 and S10 respectively);

to accommodate a changing sediment reservoir age (ΔR) through the Lake Towuti sequence (12), a Delta R with the prior U(0,1500) was used (Tables S2-S5).

Synchronizing radiocarbon and ice core chronologies

To compare our $\Delta^{14}\text{C}$ record to independent estimates of cosmogenic radionuclide production we used the ice core ^{10}Be -stack as compiled by ref. (34). For such a comparison, we need to explore i) timescale differences between our ^{14}C and ice core ^{10}Be -records, ii) differences that may arise from a different state of the carbon cycle, specifically the deep ocean ventilation, and iii) differences that may arise from either a so-called “polar bias” of the ^{10}Be -record, or a different sensitivity of ^{14}C and ^{10}Be production rates to variations in the cosmic ray flux as predicted by some production rate models (38).

Using 500 realizations of our $\Delta^{14}\text{C}$ record as the atmospheric input, we modelled ^{14}C -production rates using a box-diffusion carbon cycle model (39, 40). For each realization we determined for which combination of i) timescale shift, ii) state of deep ocean ventilation (constant values of the model’s ocean diffusivity parameter from 10% to 100% preindustrial in steps of 10%) and iii) scaling of the ^{10}Be record we obtain the best fit (lowest root mean square error) between $p^{14}\text{C}$ and ^{10}Be . The resulting histograms are shown in Fig. S15 (panels B-D). The most likely combination of parameters (applied in panel a) is i) a timescale difference of 265 years (GICC05 being younger), ii) a less efficient mixing of the deep ocean (70% its preindustrial value), and iii) a scaling of ^{10}Be by a factor of 1.3 (indicating a slight polar bias or lower sensitivity of ^{10}Be to variations in the cosmic ray flux). These findings are in excellent agreement with earlier findings (34) but significantly more precise owing to our high-quality and high-resolution truly atmospheric ^{14}C record.

The Earth’s geomagnetic field during the Laschamps Excursion

The Laschamps paleomagnetic record from the Black Sea is the best dated and most detailed record of this excursion from the Northern Hemisphere (41-43). Its age model is constrained by 16 AMS ^{14}C ages, improved by fine-tuning high-resolution records of IRD (ice-rafted detritus) counts as well as records of element ratios of Ca/Ti and K/Ti obtained from XRF (X-ray fluorescence) scanning of Black Sea sediments to the NGRIP oxygen isotope record (41, 42) on the Greenland Ice Core 2005 (GICC05) chronology (43, 44). A detailed analysis of an improved paleomagnetic record of the Black Sea paleomagnetic data, spanning from 14.5 ka to 68.9 ka, has been performed by Liu *et al.* (45). By comparison of relative paleointensity data to absolute paleointensity data (42, 46, 47), a full-vector paleomagnetic record can be established. Then, the three spherical vector components (inclination, declination, absolute intensity) were transformed into Cartesian components with one of them being oriented along the direction expected from a pure geocentric axial dipole. Most of the field decay is seen in this component. Perpendicular to it, in the second component in East-West direction and in the third component in the vertical North-South plane, only multipolar components are seen. These exhibit much smaller oscillations, but of more or less persistent amplitudes across the excursion. This means that the field decay is mostly related to the dipole component which is a global signal. Similar to the first study (41) a correction factor of $14.52 \times 10^{22} \text{ Am}^2$ was used to convert relative paleointensities into Virtual Axial Dipole Moments (VADM). The lowest field values during the Laschamps recorded in Black Sea sediments were obtained for the N-R transition at 41.63 ka with VADM values as low as $0.48 \times 10^{22} \text{ A m}$, just **~6.3%** of the modern axial dipole moment in 2010 with

$7.628 \times 10^{22} \text{ A m}^2$ (according to the 11th generation International Geomagnetic Reference Field, IGRF-11) (48). For the fully reversed phase of the Laschamps from 41.35 to 41.11 ka the VADM recovers to a mean value of $2.12 \times 10^{22} \text{ A m}^2$, about 28% of the modern axial dipole moment, and then drops down to $1.14 \times 10^{22} \text{ A m}^2$ at 40.95 ka during the R-N transition. An intermediate VADM value of around $4.00 \times 10^{22} \text{ A m}^2$ is then reached at about 40.23 ka with directions already according to a normal polarity. The field minima bracketing the Laschamps fully reversed phase were asymmetric not only in terms of field strength, but also having different durations. If a large directional precursor is taken into account then the full N-R transition took around 1000 years (41), while the R-N transition-related minimum lasted only about 2-300 years (Fig. 1). In general, the Black Sea paleointensity record conforms with other (less detailed) paleointensity stacks, such as the GLOPIS75 (49) and is therefore considered appropriate for comparison to the sequences reported in this study.

Atmospheric impacts of geomagnetic changes associated with the Laschamps Excursion

The Earth's Radiation Environment

To gauge the likely impacts of Laschamps on multiple geophysical parameters, we have used previous solar, cosmic ray, and space research studies and examples as a guide (Fig. 4). In the present epoch, the geomagnetic field prevents a large proportion of the cosmic radiation $< 14 \text{ GeV/nucleon}$ from accessing the atmosphere. During the Laschamps however, the greatly reduced geomagnetic field strength meant that nearly all of the cosmic radiation reaching the orbit of Earth gained access to the atmosphere. In addition, solar activity (the sunspot cycle) results in up to orders of magnitude changes in the radiation reaching Earth with observed periodicities $11 < T < 10000 \text{ y}$. All these variations will influence the tropospheric and stratospheric ionization.

There are two major sources of cosmic radiation that produce the ionization in the atmosphere that influences the ozone column and UV incident on Earth. They are the galactic and the solar cosmic radiation. The galactic cosmic radiation (GCR) originates in supernova throughout the galaxy; has an average age of 2×10^6 years; an energy spectrum approximating $E^{-2.65}$ and has been essentially invariant over the past 100 ka. The spectrum is referred to as the “local interstellar spectrum”, and has now been measured *in situ* by the Voyager 1 spacecraft that exited the solar system in 2012 (44). The second source is the explosive acceleration of cosmic rays following the annihilation of portions of the extremely strong sunspot magnetic fields in large solar flares. Solar cosmic radiation has a vastly different spectrum from that of the GCR, sometimes approximating E^{-6} , and intensities at energies at and below 10 GeV that can be many orders of magnitude greater than those of the GCR (45). These short-lived events, ranging from 1 to 10 days, are referred to as “solar energetic particle” (SEP) events (previous acronym SPE for solar proton event). Around 71 SEP have been observed by ground level detectors since 1942, and hundreds by satellite detectors since 1963, making their characteristics well known. Based on that knowledge we use the SEP event of 23 February 1956, the largest event observed since 1942, to estimate the effects of SEP during the Laschamps (Fig. S16). Based on neutron monitor and ionization chamber (ground level) records for the interval 1942-2012 (45) we estimate that there were approximately 3 SEP per decade with intensities within a factor of ten of those displayed in the figure. Studies of several SEP events since 1942 indicate increases in atmospheric ionization on the order of 90 times (46), which would have had far more impact at

equatorial and low latitudes during the Laschamps due to the reduced geomagnetic cut off energies. The visual impacts on the atmosphere during the night during these SEP periods may have been considerable. Cosmogenic data indicate that there have been “super-SEP” events in the past with fluences up to 40-50 times those in Fig. S16 with a frequency of about two per millennium (47, 48).

The variability and intensities of both the GCR and SEP are strongly dependent on solar magnetic activity (“the sunspot cycle”). The very tenuous low energy “solar wind” transports the solar magnetic field to the limits of the solar system, at the termination shock 120 astronomical units (1AU= distance from Sun to Earth) from the Sun. En route, the solar magnetic field partially reflects and also decelerates the GCR (“modulation”), resulting in substantial variations in the intensity reaching Earth. Historical optical observations going back to Galileo (1609) and before that to the Chinese (to 3Ky BP), show that there is a persistent ~11 year periodicity in solar activity. In addition, there have been repeated periods of “Grand Minima” (26 in the past 10ka, each of duration 40-140 years (49) when there were very few sunspots – the Spörer (CE 1400-1540), Maunder (CE 1645-1715) and Dalton (CE 1790-1820) Minima being the most recent and intensively studied using cosmogenic isotopes and sunspot records. During these intervals the solar-driven interplanetary magnetic field decreases greatly allowing the interstellar cosmic radiation to reach Earth with little attenuation. This effect is usually quantified by the parameter ϕ , the modulation potential, measured in MeV. In the present epoch ϕ varies in the range $400 < \phi < 1400$ MeV between sunspot minimum and maximum. Studies of the radiogenic radionuclides (^{10}Be , ^{14}C and ^{36}Cl) have indicated that ϕ approaches zero during Grand Minima, and the cosmic ray intensity at Earth then approximates the interstellar value (49).

During periods of high solar activity (*ie* high ϕ) the GCR intensity reaching earth is strongly decreased, but the sunspot size and sunspot magnetic field strengths are much greater, resulting in powerful solar flares, and very intense SEP events. The overall radiation environment at Earth surface during the Laschamps is summarised in Fig. S16. When the Sun is inactive, particularly during Grand Minima, the GCR intensity is persistently high for periods of 30-140 y (the $\phi=0$ curve), and there are no SEP events. When the Sun is active, the average ϕ approximates 800 MeV and the GCR intensity is low. However, very intense short-lived SEP events occur with a frequency of about three per decade. The differential spectra for the 23 February 1956, and 12 November 1960 SEP events are given in Fig. S16 and are discussed below.

A substantial fraction of both the GCR and SEP cosmic radiation is deflected from reaching Earth by the geomagnetic field. The lowest “cut-off” energy that can reach geomagnetic latitude λ in a dipole field is given by the Stoermer equation $E_{co} = 10 (M/M_0) \cdot \cos^4 \lambda$ MeV where M and M_0 are the geomagnetic dipole magnetic moments for the period of interest and the modern value, respectively. The cutoff energies for $M=0, 0.1M_0$, and M_0 for $\lambda=45^\circ$ are given in the lower left-hand axis of Fig. S16. For each value, all the radiation to the right of the symbol is accessible to the atmosphere. Comparison of the $\phi = 0$ MeV and 800 MeV curves shows that the combination of the Grand Minimum (ϕ going from 800 to ~0 MeV) and the reduction in the geomagnetic moment to $0.1 M_0$ during Laschamps results in an increase in the radiation entering the atmosphere of 1-2 orders of magnitude. Using the well-known range-energy relationship for protons in air, the scale in the top left-hand upper corner shows that the greatest increase during “Grand Minima” occurs in the “ozone layer” in the lower stratosphere below 32 km.

Consider now the difference between the GCR curve during active solar conditions ($\phi = 800$ MeV) and the two SEP spectra. For $M=0$ the 10 to 1000-fold SEP enhancements are primarily in the upper troposphere. For $M = 0.1 M_0$, three to five orders of magnitude enhancements occur in the lower stratosphere. While large SEP events only occur on average at about three per decade, calculations show that these intermittent pulses of radiation result in greater increases in the stratosphere than associated with the Grand Solar Minima.

We stress that the substantial increases in cosmic ray intensity, and the resulting large increases in ionization in the troposphere during the Laschamps occurred primarily at equatorial and low latitudes; there were minimal increases in the polar and mid-latitude troposphere. Conversely, there were substantial increases in ionization in the stratosphere at all latitudes. During the period of increased atmospheric ionization, the elevated production of nitrogen and hydrogen oxides would have resulted in a decrease in the concentration of ozone in the stratosphere, leading to a substantial increases in the UV levels on Earth (50). The marked increases in ion density in the troposphere may have acted as nucleation centers for rain and clouds, potentially impacting rainfall, cloudiness, temperatures, and ocean circulation in equatorial and mid-latitudes (51).

The cosmic radiation inputs to SOCOL and associated models used to estimate UV incident on Earth during the Laschamps

Ice-core records of ^{10}Be fluctuations at four polar locations during the Laschamps provide a well resolved record of the cosmic ray intensity from 45-39ka. Fig. 1 presents those data for 44.5-39.5ka showing a number of distinct peaks consistent with Grand Solar Minima, both in duration and spacing. During the ~ 1.6 ky period of Laschamps (42.35-40.75ka) with $M < 0.1 M_0$, there appear to have been around nine Grand Solar Minima of total duration ~ 1000 y, with five particularly intense (Fig. 1). We note that the two most intense Grand Solar Minima occurred during the latter part of the Laschamps, and this will be studied at a later time. Assuming the Sun was in an active phase between all the Grand Solar Minima, modern experience suggests that within that cumulative total 600 yr period there may have been a total of ~ 180 SEP events similar to that of 23 February 1956.

On the basis of the spectra in Supplementary Figure ##, the cosmic ray inputs to the SOCOL and associated models used to estimate the UV incident on Earth, were **TO BE REVISED**
FOLLOWING DECISIONS REGARDING THE MODELS

- (a) Nine Grand Minima events for a total of 1000 years using the $\phi=0$ MeV GCR spectrum and $M=0.1 M_0$;
- (b) 180 SEP events distributed throughout the total of 600 y between the Grand Minima, using the 23 February 1956 spectrum and $M=0.1 M_0$;
- (c) “Upper limit” cases. The estimates used in (a) and (b) are conservative and based on accurate measurements in the modern era. In addition, the geomagnetic cutoffs may have approached zero prior to and after the dipole reversal ($M=0$ in Figure ##), and “super SEP” have been observed in the cosmogenic record (Sukhodolov et al 2017; Mekhaldi, 2015). To encompass these possibilities, we have repeated (a) with $M=0$; and (b) with the SEP intensities 100 times greater than those in Figure ##, and $M=0.1 M_0$.

Auroral Zones: The balance of pressure between the solar wind and Earth's geomagnetic field results in the formation of the magnetopause (at around 10-15 Earth radii) and the geomagnetic tail of the Earth. Processes in both accelerate electrons that precipitate to earth creating the auroral zones which presently form a circle of 22 degrees in latitude radius around the geomagnetic pole (which wanders by 10 degrees or more over millennia). The reduction in dipole geomagnetic field strength to around 10% during the Laschamps would have major effects on these parameters. Estimates suggest that the magnetopause would have shrunk during the Laschamps to a radius of about 5 Earth radii during quiet periods of solar wind, and potentially to only 3 Earth radii during geomagnetic storms. As a result, the auroral zones would have shifted 10 to 20 degrees towards the equator such that they may have reached to mid or even low latitudes. Intense aurora excite oxygen emissions that are deep red, in the form of rapidly moving curtains, vertical rays, etc. It is likely that these visual phenomena would have been noticed by Paleolithic human populations, and potentially even represented in artistic depictions. These parameters and approximate calculations are summarized in Fig. 4.

Defining the timing of the Adams Event using geomagnetic, ice, and kauri records

To define the onset of the Adams Event we used the first appearance of the marked peaks in ^{10}Be flux recorded in ice records consistent with solar Grand Minima (above), as this is an indication of the reduced geomagnetic field strength allowing increased amounts of ionizing radiation to penetrate to atmospheric levels. Approximately nine contiguous large fluctuations in ^{10}Be can be observed between 42.35 and 40.8ka (Fig. 1), with some peaks also apparent in ^{14}C flux. As a result, we define the start of the Adams Event at 42.35ka, while the end is demarcated by the rapid increase in relative paleomagnetic intensity at 41.56ka as the polarity reverses. This reversed polarity phase of Laschamps continued until around 41.05ka, and was followed by the final transition phase back to normal polarity which was completed around 40.85ka. The estimates of both polarity reversal and recovery have been chosen to be consistent with the reconstructed geographic position of the Virtual Geomagnetic Pole (VGP) crossing 0 degrees latitude (42, 43).

Global chemistry climate modelling

To examine the potential impact of galactic cosmic rays (GCRs) on regional and global climate we carried out a series of different simulations. Here we report the results from **three 60-year long model runs** that we consider provides insights into the impact of a Laschamps-like event on global atmospheric chemistry and climate. The differences between the three runs are only the geomagnetic field strength (B) and solar modulation potential configuration. The geomagnetic field parameters affect the energetic particles penetration depth into the Earth's atmosphere depending on the incoming energy spectrum and latitude, while the solar modulation potential steers the galactic cosmic ray flux into the planetary atmosphere. Here we use the modelling tool for Solar-Climate-Ozone Links studies (SOCOL v3.0) (52), consisting of the global circulation model MA-ECHAM5 (MPI-M) (53, 54), a modified version of the chemistry model MEZON (55-57) and coupled to the ocean model MPI-OM (58). Versions 1 and 2 of SOCOL, based on MA-ECHAM4, have been validated by Egorova *et al.* (59) and Schraner *et al.* (60). The chemical processes triggered by solar energetic particles (SEP) and galactic cosmic rays have recently been

implemented in SOCOL v2 (61). The CRAC:CRII (Cosmic Ray Atmospheric Cascade: Application for Cosmic Ray Induced Ionization) (62, 63) model was used to describe the effect and parameterize the ionization caused by GCRs in the entire horizontal and vertical model domain. CRAC:CRII is able to account for the effects of the solar activity and the geomagnetic field on ionization rates. The solar modulation potential ϕ is used to describe the deceleration of precipitating particles due to their interaction with the solar wind. The ionization rates retrieved from this model are then converted to a NO_x and HO_x production rate, since SOCOL does not treat ion-chemistry explicitly. The conversion factor for NO_x is 1.25 nitrogen atoms per ion pair (64) of which 45% yield $\text{N}(^4\text{S})$ and 55% yield $\text{N}(^2\text{D})$. The $\text{N}(^2\text{D})$ instantaneously converts into NO via $\text{N}(^2\text{D}) + \text{O}_2 \rightarrow \text{NO} + \text{O}$. For HO_x production we used the parametrization by Solomon *et al.* (65). The latter study examined the thermodynamics of ion and neutral chemistry during charged particle precipitation to describe odd hydrogen production depending on altitude and ionization rate and found values between 1.9 and 2 odd hydrogen particles produced per ion pair below 60 km altitude. The model does not include any potential effect of GCRs on cloud properties via aerosol formation (66). We use SOCOL-MPIOM (67) in T31 horizontal resolution i.e. with an approximate grid spacing of $3.75^\circ \times 3.75^\circ$ and 39 vertical hybrid sigma-p levels, terrain-following sigma levels at the bottom and isobaric coordinates aloft. The vertical co-ordinates span the atmosphere from surface to 1 Pa (~ 80 km). The chemical module treats 41 chemical species, which interact via 140 gas-phase, 46 photolysis and 16 heterogeneous reactions. MPI-OM is based on primitive equations with hydrostatic and Boussinesq approximations. Horizontal discretization is on an orthogonal curvilinear C-grid, in the vertical isopycnal coordinates are used. MPI-OM includes a dynamic and thermodynamic sea ice model.

To examine the impacts of different geomagnetic and solar conditions we performed four 60-year long model runs. All runs were set up with glacial conditions. Before the three runs were started, a 400-year long spin-up run was made under reference conditions, to ensure that the ocean-atmosphere system was in a stable state, with no large drifts in climate parameters. The Earth's orbital parameters were fixed to historic values (Table S6). The initial land surface dataset (e.g. ice cover) and ocean temperatures are from an earlier glacial simulation with ECHAM5 and were kindly provided by Uwe Mikolajewicz from MPI Hamburg (Fig. S17); this includes the presence of the Laurentide Ice Sheet. The atmosphere was run in a 'pristine' state and concentrations of greenhouse gases (GHGs) and ozone depleting substances (ODSs) are low (Table S7), resulting in a model globally averaged annual mean 2m-temperature of $\sim 284.68\text{K}$. Trace gas concentrations and solar spectral irradiance were held fixed during the entire runs. The reference run (REF) has a modern geomagnetic dipole moment, a position of the geomagnetic North Pole at 78.5°N and 291.5°E , a solar modulation potential ϕ of 800 MV, ionization rates by GCR and auroral electrons. To emulate a weakened geomagnetic field during the Laschamps, we undertook a second run (LM) where we applied zero geomagnetic field strength keeping the other parameters as in REF setup. For the third run we applied solar modulation potential ϕ of 0 MV and exclude auroral electron precipitation effects to explore the impacts arising from a weakened geomagnetic field (zero) and Grand Solar Minima (LA). For the fourth run... To eliminate the transition from the reference spin-up to the experimental conditions the first 5 years of the simulations were not used. 60 years were compared applying a two-tailed student's *t-test*. Summary plots of seasonal differences in chemistry and climate parameters compared to REF are shown in Figs. S18-S30; these include the relative erythemal dose change which was calculated by applying a RAF factor of -1.1 to relative total ozone changes. It is important to note that the mechanisms explored for the Laschamps are

several orders of magnitude greater than current solar-induced phenomena, and as result cannot explain historic global temperature trends (68-72).

Here we focus on the impact of a weakened geomagnetic field and Grand Solar Minima (LA) during the boreal winter (December-February) which exhibits the greatest impact of all the seasons. We find that NO_x increases over most of the atmosphere due to increased ionization levels from GCRs, which both is due to a higher flux of energetic particles into the atmosphere (no geomagnetic field disturbance) and a higher particle energies allowing to penetrate the atmosphere down to low altitudes (no solar modulation potential breaking down the energetic particles). The negative anomaly in the Northern Hemisphere mesosphere is due to the decrease in solar low energetic electrons. As for NO_x, the generation of HO_x increases over the entire atmosphere, down to low altitudes. However, due to the increased amount of NO_x, in the austral summer, HO_x is destroyed by reaction with NO_x to HNO₃, which is removed through for instance, precipitation, resulting in a net negative anomaly for HO_x in the austral Southern Hemisphere. Importantly, both NO_x and HO_x have been demonstrated to cause the catalytic destruction of stratospheric ozone (while also producing tropospheric ozone) (Fig. 2C) (73); the exception to this observation is over the Northern Hemisphere pole at 50-70 km altitude.

The temperature patterns (Fig. SX) are, for a large part, linked to the ozone changes. The negative anomalies in stratospheric ozone lead to a cooling effect, except where no light penetrates the atmosphere (polar night); here, the positive anomaly in ozone over the Northern Hemisphere pole is associated with a negative temperature anomaly. In contrast, the increase in ozone in the troposphere is accompanied by positive temperature anomalies, reducing the loss of infrared thermal radiation leave the lower troposphere to higher altitudes. Intriguingly, the remarkable bi-pole pattern of temperature anomalies over the Northern Hemisphere polar night (positive anomalies centred on 10-40 km versus negative anomalies at 50-80 km) cannot be explained by ozone anomalies only. We assume that the acceleration of the Brewer-Dobson circulation leads to an increased downwelling of air over the northern pole, from altitudes of 70 km down to altitudes of 20 km (74). The air, heating up adiabatically, therefore generates a significant positive temperature anomaly at lower stratospheric altitudes. The zonal wind (Fig. 2E, F) reacts accordingly. At 20 km altitude, a warm air anomaly over the polar region disrupts the polar vortex through a decrease in the equator-to-pole temperature gradient. This process is self-sustaining, if not self-enhancing: a disrupted polar vortex will mix with warmer extratropical air masses, warming the region further, which in turn further disrupts the vortex. This disturbance then propagates upward to high altitudes (65 km), as seen in the zonal mean wind speed. One possible cause for the acceleration of the Brewer-Dobson circulation is the increased surface (10 m altitude) wind speed in front of the most important orographic barriers (for instance, the Norwegian Alps, the central Rockies, Kamtchatka, and Japan) (Fig. SXX) (75). Here, increases in the wind stream above the orography will generate additional gravity wave drag, potentially vertically propagating into the stratosphere and driving the ‘extratropical pump’. Our modelled sea-level pressure increase over the Arctic and North America and decreases over western Europe corresponds to a negative phase of the Arctic Oscillation (AO) and/or a positive North Atlantic Oscillation-like pattern (NAO), consistent with contemporary studies that have linked persistent solar minimum-induced long-term changes in these modes (76).

A short paragraph to be added here for the SEP model outputs

Potential impacts of VGP route

The inferred geographic route taken by the Virtual Geomagnetic North Pole (VGP) during the Laschamps (41-43) is shown in Fig. 2. In summary, the VGP initially moved eastwards across northern North America (over the Laurentide Ice Sheet; LIS) as far as the northern Atlantic and Greenland (around 42.25ka) before reversing track across central North America (and the LIS once more) back to the northern Pacific Ocean (around 41.80ka). The VGP then moved rapidly southwards over the Pacific as far as Antarctica (around 41.51ka) before crossing the southern continent and exiting south of Western Australia (around 40.35ka). The return route of the VGP northwards through the Indian Ocean was only slightly slower than the Pacific leg, and reached mid-Eurasia by 40.83ka. The northwards movement then continued to the current Arctic position of the VGP. It is notable that this route took the VGP across or close to many sites in our Pacific transect recording climatic or biotic impacts during the Laschamps. These sites include Auckland Island, New Zealand, the Australian mainland, New Caledonia and to a lesser extent Sulawesi. One interesting possibility is that the reduced geomagnetic field strength expressed directly above the VGP may have allowed increased amounts of ionizing radiation to penetrate to the local atmosphere, with ensuing enhanced climatic and biological impacts. In this regard it is potentially important that the change in ice sheet growth rate of the LIS (from retreat to rapid expansion) occurred very close in time to when the VGP passed by geographically, around 42.3-42.2ka in eastward and then westward transects (77-79). The timing suggests the ice sheet response may have been amplified by the location of the VGP, and closely corresponds to the timing of the shift in ITCZ (Lake Towuti), Southern Hemisphere westerlies (Auckland Island), and increased aridity suggested across Australia (Lake Mungo and Lynch's Crater). To date, the potential local impacts of VGP position has not been included in the climate modelling runs.

Summary of environmental and archaeological changes during the Adams Event

Note: All radiocarbon ages reported in this study have been calibrated using the new combined kauri-Hulu Cave calibration dataset.

Potential signals in Greenland ice records: In the Northern Hemisphere around 42ka, the Adams Event and broader Laschamps appears to be associated with a rapid re-expansion phase of the Laurentide Ice Sheet from a glacial minima that included an ice-free Hudson Bay (77-79). Analyses of Greenland ice records have revealed atypical signals in the stadial (GS-10) and interstadial (GI-9) events that occur during and following the Laschamps. The relatively insubstantial GS-10 signal is absent or only weakly recorded in many other climate records, including marine signals such as Cariaco Basin, Arabian Sea, and Iberian Margin, and has an unusually low signal of atmospheric dust in Greenland ice records (80, 81). The ensuing GI-9 has an unusually gradual onset while the WAIS Antarctic ice record shows minimal evidence of a corresponding Antarctic isotope maximum event at this time, which would be anticipated from a bipolar seesaw response (82). This has led to suggestions that GI-10 and GI-9 in fact represent a single longer interstadial event that has been interrupted by a pronounced cold phase that was not a true D-O stadial, but which altered the temperature gradient between the mid-latitudes and Greenland (80, 81). This would be consistent with the strengthened polar vortex during the Adams Event causing expansion of sea ice around Greenland, and producing a local signal recorded as GS-10. Importantly, the enigmatic GS-10 event occurred at exactly the same time as the weak geomagnetic field strength of the final transition phase of Laschamps (Fig. 1). A further

observation is that the Adams Event itself is closely coincident with the prolonged cold period of GS-11, while the Laschamps reversed polarity phase overlaps markedly with interstadial GI-10. Together, the coincident timing of these events raises the prospect that marked cooling signals corresponding to periods of low geomagnetic field strength during the Laschamps may be preserved in Greenland ice records, but that they have not been previously identified due to the lack of dating resolution, and close resemblance to the pattern of surrounding stadial-interstadial events.

Subantarctic environmental changes: The pollen and spore results from the lower organic unit in Pillar Rock indicate a shrub-grassland, dominated by *Dracophyllum longifolium* and tussock grasses (Fig. S6). An extinct pollen type – which we are here calling ‘*Pseudopanax moarii*’ – almost certainly represents a close relative of the *Pseudopanax* group of large leaved small trees on the New Zealand mainland. Megaherbs were present and for most of the sequence the local ground surface was a *Plantago* sward. Interpretation is complicated by the fact that the site is currently on an exposed cliff subjected to strong winds and thus in tussock grassland, while shrub and forest cover is some 200 m distant downslope. The extant vegetation cover is therefore strongly influenced by wind. Growth of a *Dracophyllum* shrubland close to the cliff edge, and the absence of stones in the sediments implies reduced gale force winds. The annual temperatures at the time cannot have been much lower than those of the present. The upper peat sequence, covering the transition from the full glacial to the beginning of the Holocene, is initially dominated by megaherbs and relatively low levels of grass with almost no woody plants. This is typical of much higher elevation sites above 250 m and with estimated annual temperatures at least 1.5 °C lower than at current sea level.

The lower half of the sequence, centered on 52ka has consistent representation of pollen from the tall New Zealand endemic podocarp trees *Prumnopitys taxifolia* and *Dacrydium dacrydioides*. These trees are abundant in mainland lowland forests and their long-distance transport to Auckland Island indicates substantial areas of lowland forest in southern regions of New Zealand. This period coincides with the highest levels of woody plants and lowest of grasses at the site and thus indicates peak warmth. Mean annual temperatures at this time were likely to have been within 1.5 °C of the present. From 50 ka onwards, the long-distance pollen assemblage consists of Nothofagaceae, *Phyllocladus*, *Halocarpus* and Australian sourced types such as *Casuarina* and *Eucalyptus*. Locally, grasses increase and woody plants decline indicating increasingly cooler climates. Mean annual temperatures at the time of deposition of the lower organic band were probably within 1.0 - 1.5 °C of the present. The subsequent influx of silt, stones and boulders indicates severe periglacial activity, followed from 11.5 ka by stabilization of the ground surface but with a megaherb dominated vegetation cover typical of that above 300 m elevation on the current landscape. Lack of stones and silt in the peat suggest relatively weaker westerly winds. Shortly after increase of *Myrsine* shrubland at 8 ka, influx of stones and silt recommenced, indicating a resumption of intense westerly gale-force winds. The summary pollen record from the early Holocene upper organic unit is shown in Fig. S8.

Equatorial West Pacific changes: The sediment deposits in Lake Towuti, Sulawesi, demonstrate a marked shift in $\delta^{13}\text{C}$ (leaf wax) to more negative values (depleted in ^{13}C) in close association with a minimum in geomagnetic intensity (21). Radiocarbon dates through this period align well with the magnetic changes, and indicate a transition at 42 ka (Fig. S11). These signals indicate

increasing environmental aridity, which has been suggested to be a consequence of migration of the ITCZ south (12) and the general conditions remained in place until the Holocene (comparable to the onset and duration of inferred periglacial conditions on Auckland Island). Similarly, on New Caledonia (which was uninhabited in the Late Pleistocene) a change in vegetation from *Araucaria* to more arid conditions around this time (83) parallels the patterns seen in Australia and Sulawesi.

Megafaunal extinctions: High-resolution Pleistocene records of biodiversity change appear quite episodic. A key example is megafaunal extinctions, which appear to be staggered throughout the late Pleistocene (84) in many areas. Interestingly, within this generally distributed pattern, a cluster of megafaunal genetic transitions (woolly rhino, mammoth, bison) were previously observed around the timing of the Mono Lake geomagnetic excursion (84). Importantly, a global trend is that megafaunal extinctions seem to occur long after the arrival of modern humans in given areas such as Eurasia, the Americas (85), and even large islands such as Madagascar (86). The global pattern of extended human overlap with megafauna, and lack of intensive signs of megafaunal hunting, makes it increasingly hard to explain humans as the primary cause of extinctions. Australia is an extreme example with an overlap of Anatomically Modern Humans (AMH) and megafauna of at least ~10 ka, if not more (87, 88). The discovery that the Laschamps is contemporaneous with climatic shifts to arid conditions and megafaunal extinctions in Australia raises interesting questions about potential causes. Many studies have pointed out that global megafaunal populations have survived numerous previous glacial cycles, suggesting that something must have been different in the last cycle, with the appearance of AMH being the most likely key factor. In the Australian situation, a model where the Adams Event led to major environmental shifts including increased aridity could allow a critical resource *e.g.* water supplies, to be occupied or dominated by humans, resulting in outsized impacts on megafaunal populations without a marked increase in human population size or activity. Recent modelling work has favored such a model to explain the Australian megafaunal extinctions at 42 ka (89, 90). Similarly, fires from increased lightning strikes, potentially increased by atmospheric ionization during the Adams Event, and other consequences of the climatic changes may have played significant roles and could explain increased charcoal levels in sites such as Lynch's Crater from 42 ka (91). It is worth noting that many large Australian endemic terrestrial taxa that survived this megafaunal extinction phase show relatively limited genetic diversity, such as the thylacine, whose mitochondrial diversity indicates an origin around 42 ka (92). This suggests that even surviving large animal populations may preserve genomic signals of population bottlenecks due to the impact of the Adams Event.

Neandertal extinction: The extinction of European Neandertal populations appears to have occurred in a temporally and geographically staggered pattern moving across Europe from east to west (93-96). This pattern has been modelled as resulting from the westward spread of steppe landscapes and permafrost zones during the intense cold spells of Greenland Stadials 12 and 10; 44.3-40.8ka) in combination with the arrival of AMH from eastern Europe (93, 94). Stalactite records from the East Carpathians used to support this model reveal a prolonged period of extreme low summer temperatures that spanned from GS-10 through into GS-9 and subsequent Heinrich Event (HE) 4, despite the interstadial GI-9 recorded in Greenland ice records (93). This period of low summer temperatures commences with the latter phase of Laschamps, and was accompanied by shifts in conditions across Europe to increased aridity, altered biomes and

changed seasonality in areas such as the Black Sea. Importantly, these environmental changes were accompanied by widespread depopulation and archaeologically sterile layers in western Europe lasting several centuries, which separate the earlier Chatelperronian (Neandertal) from the later Aurignacian (AMH) layers. This disjunct stratigraphy has been used to suggest the immediate cause of Neandertal extinction may not have been direct competition, but better or more rapid environmental adaptation by invading AMH into environments vacated by Neandertal populations during these periods of cooling induced environmental change (93). Importantly, this prolonged period of environmental change overlaps with Laschamps, which our model suggests should have induced cooling conditions. Together with the preceding extreme cold stadial GS-12, this suggests the impacts of the Adams Event and broader Laschamps on climate and environments may have been sufficient to negatively effect the remaining Neandertal populations, perhaps due to their dietary specialization of terrestrial animals, allowing invading AMH populations to increasingly occupy their former range. While it has been suggested that a higher UVB sensitivity of Neandertals might have led to their extinction during the Laschamps (50), the associated climatic and environmental changes seems a far more plausible explanation given the wide range of melanian pigmentation alleles observed in Neandertal individuals (97).

To test whether the extinction of Neandertals was contemporaneous with either the Adams Event, or Laschamps in general, we re-calibrated a recent compilation of high-quality radiocarbon dated specimens that represent last occurrences at different Neandertal sites, using the kauri-Hulu calibration curve reported here. Using the OxCal Phase function (36, 37), we calibrated published radiocarbon age estimates from bone collagen (ultrafiltered) (95, 96) to refine the estimated age of Neandertal extinction to 40.9-40.5ka at 1σ (41.0-40.3ka at 2σ), which overlaps with the final transition phase to normal magnetic polarity 41-40.8ka and the enigmatic GS-10 event. (Fig. S20). Comparisons of early AMH cultures in Europe that overlap with Neandertals have shown that the Uluzzian in Italy also ends contemporaneously at this point (93), indicating the Laschamps may have also negatively impacted AMH populations in Europe at the time. A warmer period leading up to the Laschamps in the Northern Hemisphere locations might also explain why the archaeological record appears to indicate that multiple Arctic sites were occupied by AMH populations relatively rapidly after the 50-55 ka colonization of Eurasia. The cold conditions following Laschamps, and leading into the LGM, may have limited the ability of AMH to survive at such northern sites e.g. the Russian early paleolithic site of Mamontovaya Kurya (98).

Human movement and behavior in Sahul: The human burials at Mungo Lake, Australia, which have been dated by Optically Stimulated Luminescence (OSL) analysis of the sand layers in which they were buried, are within or close in age to the Adams Event (99). The Mungo I skeleton is bracketed by OSL ages of 42.7 and 42.5 ka, while Mungo III is similarly constrained at 42.2 and 41.9 ka, with errors on all dates around 2.5 k (99). Stone tools are recorded in older layers, with a maximum age at the site of 50 ka, similar to many other early sites around Australia (88). The human burials are close to the time when climatic patterns appear to have changed in the Mungo stratigraphy, marked by gravel layer III, dated around 42 ka. Given the much earlier occupation by humans of this site, it is intriguing as to why the burials themselves seem to be limited to the time of the Adams Event. Around the same time, Timor Leste was first occupied, with evidence of cave habitation and red ochre use around 42 ka (100, 101). The role of decreasing global sea level (in response to the rapid growth of the Laurentide Ice Sheet

growth) (77, 78) in allowing AMH exploration of Timor Leste and the wider region remains unclear.

Southern African records: A key vertebrate fossil archive from the southern Cape of South Africa shows that the magnitude of large mammal faunal change across the Laschamps exceeded that which occurred across the Pleistocene-Holocene transition, and corresponded with expansion of C₄ grassland and shifting westerly airflow, suggesting hemispheric-wide impacts (102). The southern Cape of South Africa, which includes the region encompassing the southern coastal plains and the east-west trending ranges of the Cape Fold Belt, is uniquely positioned to inform on the history of temperate and tropical circulation systems in the region because it receives winter rainfall from frontal systems associated with the westerly storm track as well as summer rainfall related to tropical easterly flow (103). Multiple lines of evidence from the region's fossil and climatic archives highlight significant changes that correspond in age with the Adams Event.

The archaeological deposits at Boomplaas Cave (104) provide the only southern Cape mammalian fossil record that encompasses the Adams Event (Fig. S21) (105). At this site, the faunas from stratum BP, the earliest ¹⁴C ages for which are ~40.3 ka (106), are distinct from those found in overlying and underlying stratigraphic intervals (105). This is shown here in Fig. S21, which plots chord distance across adjacent pairs of stratigraphic units (see 107), and indicates that the magnitude of faunal change across the transition to and from stratum BP exceeds that which occurred across the Pleistocene-Holocene transition. Stable carbon isotope ($\delta^{13}\text{C}$) evidence indicates elevated consumption of C₄ grasses by BP grazers (108), matching a positive excursion in $\delta^{13}\text{C}$ in the nearby (~4 km east) Cango stalagmite (109). The onset of this excursion in the Cango record is ~41 ka (Fig. S22) though it may be closer to ~42.5 ka if the radiocarbon reservoir correction applied by ref. (109) is too large (110). The implication of these archives is an expansion of C₄ grassland immediately following the Adams Event, likely reflecting greater influence of summer rainfall and relatively less influence of winter precipitation systems delivered by Southern Hemisphere westerly airflow (108).

Cave Art: The earliest cave art in ISEA overlaps with the Adams Event (from 42 ka; Fig. S23), and AMH cave art appears in Europe almost contemporaneously (111, 112). The coincidence has been noted, and regarded as currently unexplained (111, 112). Similarly, sites in Timor Leste, and Southeast Asia more generally, show an onset of cave habitation and red ochre use around 42 ka (100). The relatively sophisticated nature of the early cave art suggests that figurative painting was already well-established prior to it being recorded on cave walls, presumably on other substrates such as rock shelter or cliff walls or other materials (e.g. wood, bark shields), but that these have not survived subsequent (long term) environmental exposure. The globally common appearance of negative and positive ochre hand stencils in Laschamps-aged cave art is also interesting given the utility of red ochre-based skin coverings as protection against ultraviolet radiation, which is still practiced in places such as Africa (113). In terms of the potential use of ochre skin coverings as a sunscreen it is also possible that in temperate areas such as Europe where animal skins are likely to have been routinely used, hands and arms would have been an important area for ochre sunscreen application. If applied by blowing (e.g. through a straw, or from the mouth), then a negative stencil would have been a routine consequence and may have been adopted as an artistic feature. Either way, the contemporaneous appearance of

hand stencils and complex art in different parts of the world would appear to represent the first detection of the activity, rather than the origin of the behavior itself as has sometimes been suggested, particularly with reference to the origins of cognitive thought and language. In a similar fashion, the apparent origins of other behavior suddenly recorded in cave deposits at 42 ka, such as deep ocean fishing in Timor Leste (*100*), might represent the same preservation bias due to the more intense utilization of cave environments. Again, this would suggest that the behaviors themselves could considerably precede 42 ka.

The earliest AMH artistic depictions involve red ochre hand stencils, symbols and figurative animal art in both Europe and ISEA. In El Castillo cave, Spain, a large stippled red disk near a series of such images (Panel de las Manas) has been dated by overlying stalactites at >41.4ka (*114*), and represents the earliest figurative art currently known in Europe. Given the temporal proximity to Laschamps, this raises the question of whether the curving series of large red disks observed in El Castillo could potentially represent the movement of the sun (or moon), whose appearance and damaging UVB outputs are likely to have changed significantly and rapidly during this period of time. Intriguingly, a second large red disk image from another gallery of such images in El Castillo (Galeria de los Discos) was also dated in the same study, and was tightly bracketed between 34.2 and 35.7ka (*114*) (Fig. 3), which overlaps the Mono Lake geomagnetic excursion 34.5k). This would appear to add further support to the idea that these images are related to phenomena during geomagnetic excursions, and that this behavior shows some continuity over a periods of at least 7ka. In addition to potential images of the sun or moon, such phenomena are likely to relate to the reduced magnetosphere diameter during such excursion events, which would have allowed aurora to spread to low latitudes, **potentially ? 30°**, including southern Europe. During solar Grand Minima or Solar Energetic Particle events these atmospheric conditions are likely to have been far more extreme (Fig. 4). Intense auroral conditions excite oxygen which produces deep red emissions, and it is highly likely that intense and unusual auroral visual phenomena would have made a considerable impression on human populations who observed them, potentially then being reflected in artistic depictions. It will be important to perform largescale dating studies on cave art to investigate whether visual styles or images might be potentially related to geomagnetic excursions. This could potentially include analysis of the magnetic signals preserved in the ochre itself.

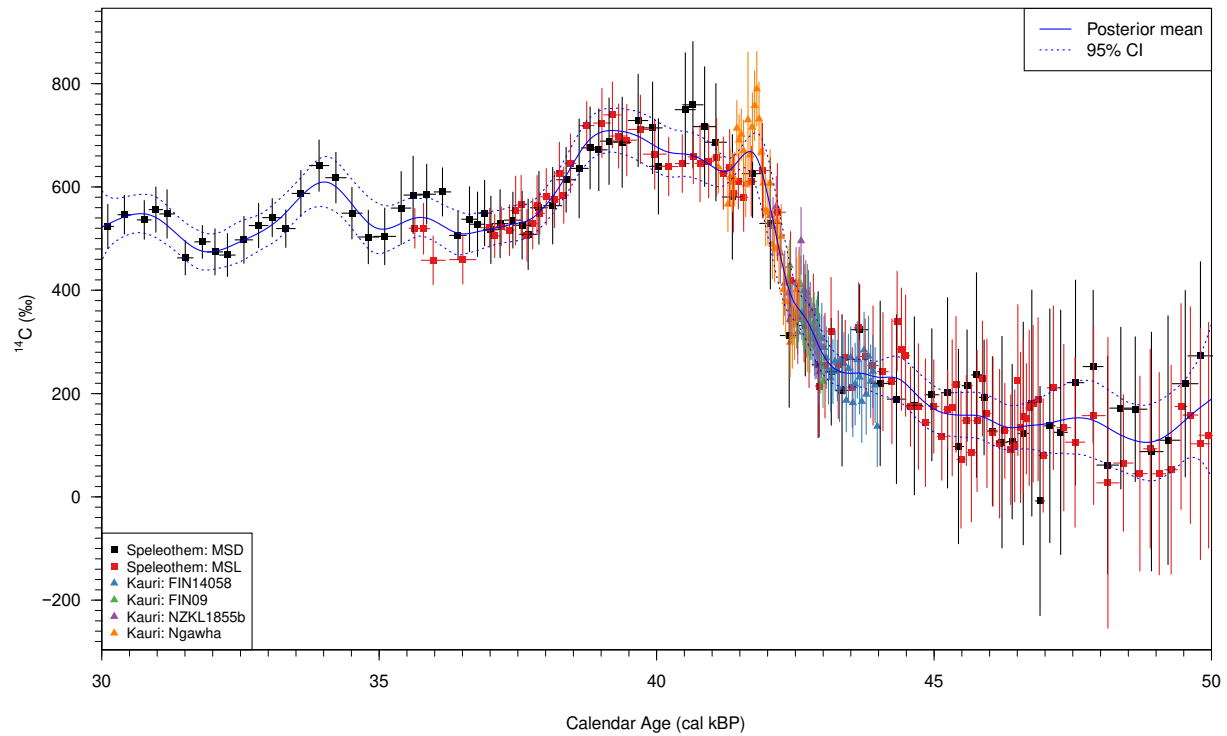


Fig. S12. Posterior mean of the kauri-Hulu Southern Hemisphere radiocarbon calibration curve from 30-50 ka in $\Delta^{14}\text{C}$ space together with its 95% credible interval.

All $\Delta^{14}\text{C}$ observations are shown with their 95% probability intervals. The four floating kauri trees are located at their posterior mean calendar ages as estimated during curve creation. The data from the two Hulu speleothems (MSD and MSL) are plotted at their prior calendar age estimates based upon U/Th dating (shown with 95% probability intervals) and adjusted in $\Delta^{14}\text{C}$ by the posterior mean offset to the Southern Hemisphere kauri estimated in curve construction. Repeat ^{14}C measurements within MSD and MSL have been combined (using a weighted $F^{14}\text{C}$ mean) before plotting.

Kauri-Hulu Laschamps Calibration Curve

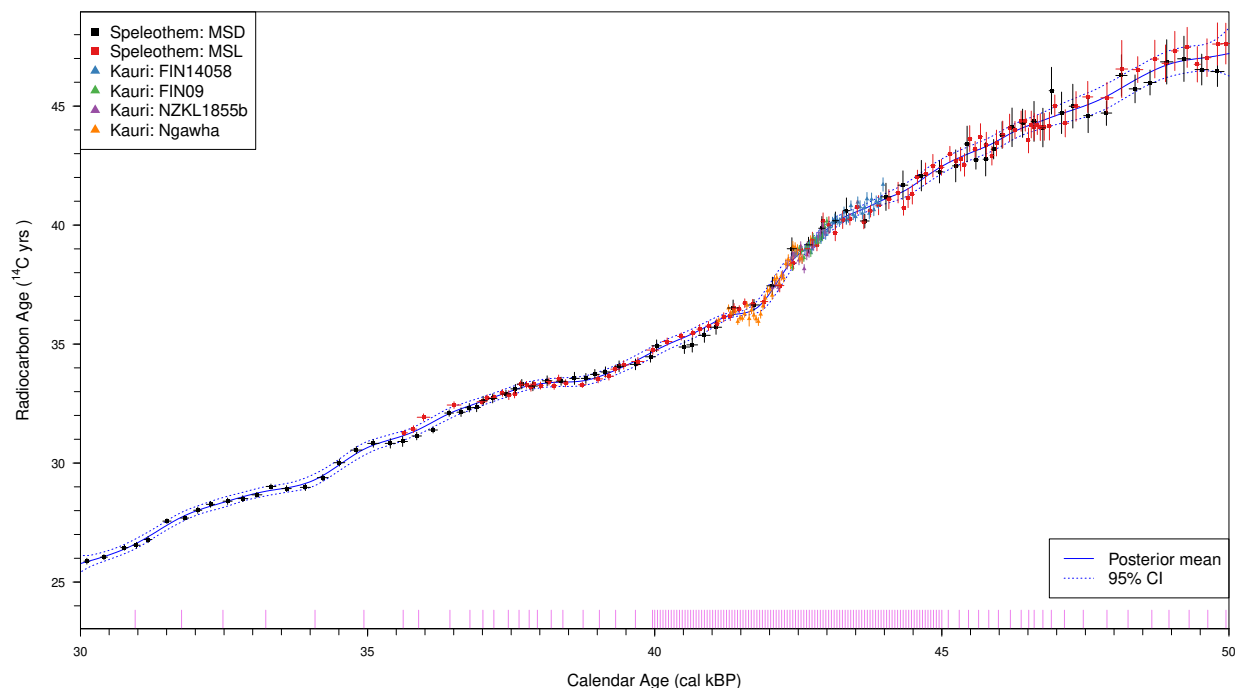


Fig. S13. Posterior mean of the kauri-Hulu Southern Hemisphere radiocarbon calibration curve from 30-50 ka in radiocarbon age space together with its 95% credible interval. The data are shown with their 1σ uncertainties in both radiocarbon and calendar age. Shown as a rug along the bottom are the knot locations for our spline, with the higher density of evenly-spaced knots covering the potential calendar ages of the four kauri floating trees. As in Figure S12, the kauri trees are located at their posterior mean calendar ages (the uncertainty in these posterior calendar ages is not indicated on the plot); the Hulu speleothems their priors based upon U/Th and adjusted in radiocarbon age according to the posterior mean of the offset to the SH data estimated during curve creation. Repeat ^{14}C measurements within MSD and MSL have been combined (using a weighted $F^{14}\text{C}$ mean) before plotting.

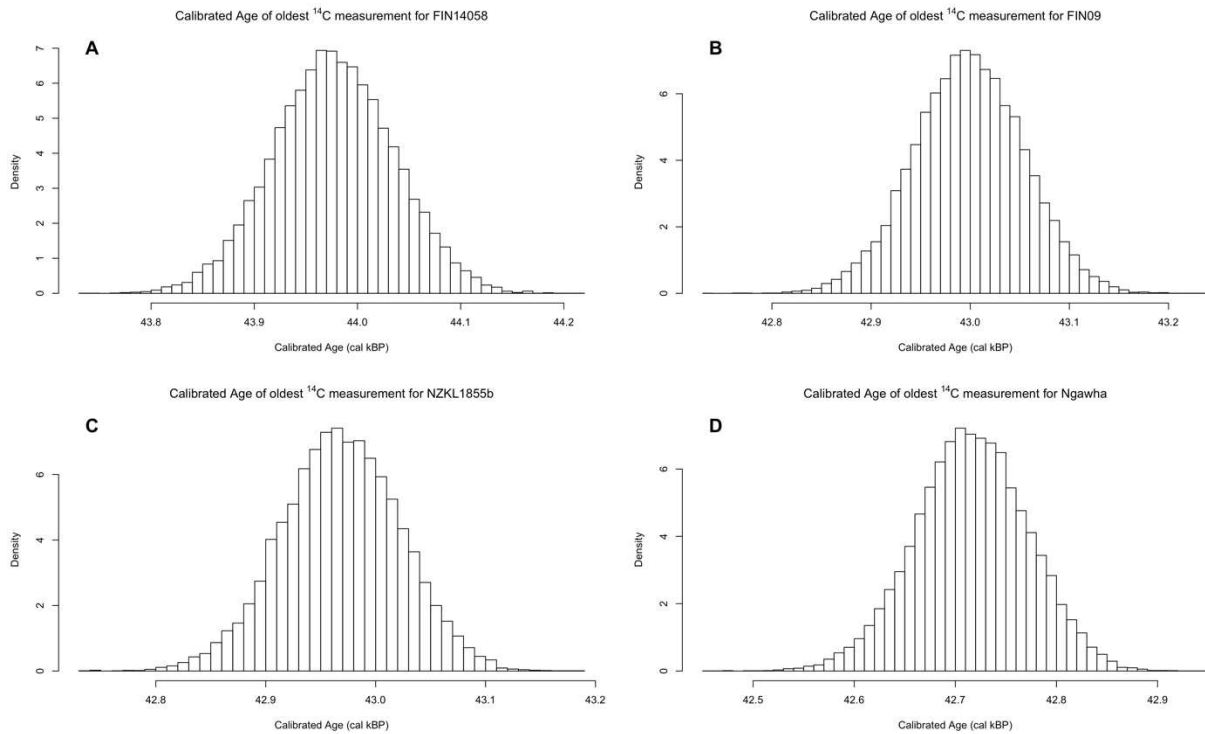


Fig. S14. Histograms of the posterior calendar ages of the oldest ^{14}C determination for each of the four kauri trees estimated during the construction of the radiocarbon calibration curve. (A) and (B) Kai Iwi Lakes trees (FIN09 and FIN14058), (C) Mangawhai (NZKL1855) and (D) Ngāwhā Springs (Nga001).

References and Notes

1. A. M. Lorrey *et al.*, The scientific value and potential of New Zealand swamp kauri. *Quatern Sci Rev* **183**, 124-139 (2018).
2. J. Palmer *et al.*, Extension of New Zealand kauri (*Agathis australis*) tree-ring chronologies into Oxygen Isotope Stage (OIS)-3. *J Quatern Sci* **21**, 779-787 (2006).
3. J. Palmer, C. S. M. Turney, A. G. Hogg, A. M. Lorrey, R. J. Jones, Progress in refining the global radiocarbon calibration curve using New Zealand kauri (*Agathis australis*) tree-ring series from Oxygen Isotope Stage 3. *Quatern Geochron* **27**, 158-163 (2015).
4. C. S. M. Turney *et al.*, Using New Zealand kauri (*Agathis australis*) to test the synchronicity of abrupt climate change during the Last Glacial Interval (60,000-11,700 years ago). *Quatern Sci Rev* **29**, 3677-3682 (2010).
5. P. G. Quilty, Origin and evolution of the sub-antarctic islands: the foundation. *Papers and Proceedings of the Royal Society of Tasmania* **141**, 35-58 (2007).
6. C. S. M. Turney *et al.*, Tropical forcing of increased Southern Ocean climate variability revealed by a 140-year subantarctic temperature reconstruction. *Clim Past* **13**, 231-248 (2017).
7. C. S. Nelson, P. J. Cooke, C. H. Hendy, A. M. Cuthbertson, Oceanographic and climatic changes over the past 160,000 years at Deep Sea Drilling Project Site 594 off southeastern New Zealand, southwest Pacific Ocean. *Paleoceanography* **8**, 435-458 (1993).
8. M. S. McGlone, The Late Quaternary peat, vegetation and climate history of the Southern Oceanic Islands of New Zealand. *Quaternary Science Reviews* **21**, 683-707 (2002).
9. C. S. M. Turney *et al.*, Intensification of Southern Hemisphere westerly winds 2000-1000 years ago: Evidence from the subantarctic Campbell and Auckland Islands (52-50°S). *Journal of Quaternary Science* **31**, 12-19 (2016).
10. E. Rainsley *et al.*, Pleistocene glacial history of the New Zealand subantarctic islands. *Clim Past* **15**, 423-448 (2019).
11. P. D. Moore, J. A. Webb, M. E. Collinson, *Pollen Analysis*. (Blackwell Science, Cambridge, 1991).
12. J. M. Russell *et al.*, Glacial forcing of central Indonesian hydroclimate since 60,000 y BP. *PNAS* **111**, 5100-5105 (2014).

13. G. Hope, Environmental change in the late Pleistocene and later Holocene at Wanda site, Soroako, South Sulawesi, Indonesia. *Palaeogeography, Palaeoclimatology, Palaeoecology* **171**, 129-145 (2001).
14. E. Aldrian, R. Dwi Susanto, Identification of three dominant rainfall regions within Indonesia and their relationship to sea surface temperature. *International Journal of Climatology: A Journal of the Royal Meteorological Society* **23**, 1435-1452 (2003).
15. M. H. O'Leary, Carbon isotope fractionation in plants. *Phytochemistry* **20**, 553-567 (1981).
16. M. D. Hatch, C₄ photosynthesis: a unique blend of modified biochemistry, anatomy and ultrastructure. *Biochimica et Biophysica Acta (BBA)-Reviews on Bioenergetics* **895**, 81-106 (1987).
17. I. S. Castañeda *et al.*, Wet phases in the Sahara/Sahel region and human migration patterns in North Africa. *PNAS* **106**, 20159-20163 (2009).
18. K. A. Huguen, T. I. Eglinton, L. Xu, M. Makou, Abrupt tropical vegetation response to rapid climate changes. *Science* **304**, 1955-1959 (2004).
19. A. F. Diefendorf, K. E. Mueller, S. L. Wing, P. L. Koch, K. H. Freeman, Global patterns in leaf ¹³C discrimination and implications for studies of past and future climate. *PNAS* **107**, 5738-5743 (2010).
20. M. J. Kohn, Carbon isotope compositions of terrestrial C₃ plants as indicators of (paleo) ecology and (paleo) climate. *PNAS* **107**, 19691-19695 (2010).
21. K. H. Kirana *et al.*, A high-resolution, 60 kyr record of the relative geomagnetic field intensity from Lake Towuti, Indonesia. *Physics of the Earth and Planetary Interiors* **275**, 9-18 (2018).
22. C. S. G. Gogorza *et al.*, Paleointensity studies on Holocene–Pleistocene sediments from lake Escondido, Argentina. *Physics of the Earth and Planetary Interiors* **145**, 219-238 (2004).
23. G. Tamuntuan *et al.*, Variation of magnetic properties in sediments from Lake Towuti, Indonesia, and its paleoclimatic significance. *Palaeogeography, Palaeoclimatology, Palaeoecology* **420**, 163-172 (2015).

24. A. G. Hogg *et al.*, Dating ancient wood by high sensitivity Liquid Scintillation Spectroscopy and Accelerator Mass Spectrometry - Pushing the boundaries. *Quatern Geochron* **1**, 241-248 (2006).
25. A. Hogg *et al.*, The New Zealand kauri (*Agathis australis*) Research Project: A radiocarbon dating intercomparison of Younger Dryas wood and implications for IntCal. *Radiocarbon* **55**, 1-14 (2013).
26. A. Hogg, in *Liquid Scintillation Spectrometry 1992*, J. E. Noakes, H. A. Polach, F. Schonhofer, Eds. (Radiocarbon, 1993), pp. 135-142.
27. H. Cheng *et al.*, Atmospheric $^{14}\text{C}/^{12}\text{C}$ changes during the last glacial period from Hulu Cave. *Science* **362**, 1293-1297 (2018).
28. T. J. Heaton *et al.*, The IntCal20 approach to radiocarbon calibration curve construction: A new methodology using Bayesian splines and errors-in-variables. *Radiocarbon* **62**, 821-863 (2020).
29. P. J. Reimer *et al.*, The IntCal20 Northern Hemisphere radiocarbon age calibration curve (0-55 kcal BP). *Radiocarbon* **62**, 725-757 (2020).
30. A. G. Hogg *et al.*, SHCal20 Southern Hemisphere calibration, 0-55,000 years cal BP. *Radiocarbon* **62**, 759-778 (2020).
31. J. Southon, A. L. Noronha, H. Cheng, R. L. Edwards, Y. Wang, A high-resolution record of atmospheric ^{14}C based on Hulu Cave speleothem H82. *Quatern Sci Rev* **33**, 32-41 (2012).
32. R. A. Staff *et al.*, Reconciling the Greenland ice-core and radiocarbon timescales through the Laschamp geomagnetic excursion. *EPSL* **520**, 1-9 (2019).
33. K. A. Hughen, J. Southon, S. Lehman, C. Bertrand, J. Turnbull, Marine-derived ^{14}C calibration and activity record for the past 50,000 years updated from the Cariaco Basin. *Quatern Sci Rev* **25**, 3216-3227 (2006).
34. F. Adolphi *et al.*, Connecting the Greenland ice-core and U/Th timescales via cosmogenic radionuclides: testing the synchronicity of Dansgaard–Oeschger events. *Clim Past* **14**, 1755-1781 (2018).
35. G. Wagner *et al.*, Presence of the solar de Vries Cycle (~ 205 years) during the last ice age. *GRL* **28**, 303-306 (2001).

36. C. Bronk Ramsey, S. Lee, Recent and planned developments of the program OxCal. *Radiocarbon* **55**, 720-730 (2013).
37. C. Bronk Ramsey, Dealing with outliers and offsets in radiocarbon dating. *Radiocarbon* **51**, 1023-1045 (2009).
38. J. Masarik, J. Beer, Simulation of particle fluxes and cosmogenic nuclide production in the Earth's atmosphere. *J Geophys Res-Atmos* **104**, 12099-12111 (1999).
39. U. Siegenthaler, M. Heimann, H. Oeschger, ¹⁴C variations caused by changes in the global carbon cycle. *Radiocarbon* **22**, 177-191 (1980).
40. R. Muscheler *et al.*, Changes in the carbon cycle during the last deglaciation as indicated by the comparison of ¹⁰Be and ¹⁴C records. *Earth Planet Sci Lett* **219**, 325-340 (2004).
41. L. Jiabo, N. R. Nowaczyk, S. Panovska, M. Korte, H. W. Arz, The Norwegian-Greenland Sea, the Laschamps and the Mono Lake excursions recorded in a Black Sea sedimentary sequence spanning from 68.9 to 14.5 ka. *Journal of Geophysical Research: Solid Earth*, e2019JB019225 (2020).
42. N. R. Nowaczyk, H. W. Arz, U. Frank, J. Kind, B. Plessen, Dynamics of the Laschamp geomagnetic excursion from Black Sea sediments. *EPSL* **351-352**, 54-69 (2012).
43. J. Liu, N. R. Nowaczyk, S. Panovska, M. Korte, H. W. Arz, The Norwegian-Greenland Sea, the Laschamps and the Mono Lake recorded in Black Sea paleosecular variation records between 68.9 and 14.5 ka. *Journal of Geophysical Research*, (2020).
44. A. C. Cummings *et al.*, Galactic cosmic rays in the local interstellar medium: *Voyager 1* observations and model results. *The Astrophysical Journal* **831**, 18 (2016).
45. K. G. McCracken, H. Moraal, M. A. Shea, The high-energy impulsive ground-level enhancement. *The Astrophysical Journal* **761**, 101 (2012).
46. A. Mishev, Short- and medium-term induced ionization in the Earth atmosphere by galactic and solar cosmic rays. *International Journal of Atmospheric Sciences* **2013**, 9 (2013).
47. T. Sukhodolov *et al.*, Atmospheric impacts of the strongest known solar particle storm of 775 AD. *Sci Rep* **7**, 45257 (2017).
48. F. Mekhaldi *et al.*, Multiradionuclide evidence for the solar origin of the cosmic-ray events of AD 774/5 and 993/4. *Nature Comms* **6**, 8611 (2015).

49. K. McCracken, J. Beer, F. Steinhilber, J. Abreu, A phenomenological study of the cosmic ray variations over the past 9400 years, and their implications regarding solar activity and the solar dynamo. *Solar Physics* **286**, 609-627 (2013).
50. J. E. T. Channell, L. Vigliotti, The role of geomagnetic field intensity in late Quaternary evolution of humans and large mammals. *Reviews of Geophysics* **57**, doi: 10.1029/2018rg000629 (2019).
51. J. Kirkby, Cosmic rays and climate. *Surv Geophys* **28**, 333-375 (2007).
52. IACETH, "Documentation for the SOCOL model," (Institute for Atmospheric and Climate Science, ETH, 2009).
53. E. Roeckner *et al.*, Sensitivity of simulated climate to horizontal and vertical resolution in the ECHAM5 atmosphere model. *Journal of Climate* **19**, 3771-3791 (2006).
54. E. Manzini, M. Giorgetta, M. Esch, L. Kornblueh, E. Roeckner, The influence of sea surface temperatures on the northern winter stratosphere: Ensemble simulations with the MAECHAM5 model. *Journal of climate* **19**, 3863-3881 (2006).
55. E. Rozanov, M. E. Schlesinger, V. Zubov, The University of Illinois, Urbana-Champaign three-dimensional stratosphere-troposphere general circulation model with interactive ozone photochemistry: Fifteen-year control run climatology. *Journal of Geophysical Research: Atmospheres* **106**, 27233-27254 (2001).
56. T. Egorova, E. Rozanov, V. Zubov, I. Karol, Model for investigating ozone trends (MEZON). *Izvestiya. Atmospheric and Oceanic Physics* **39**, 277-292 (2003).
57. C. R. Hoyle, *Three dimensional chemical transport model study of ozone and related gases 1960-2000*. (ETH Zurich, 2005).
58. S. J. Marsland, H. Haak, J. H. Jungclaus, M. Latif, F. Röske, The Max-Planck-Institute global ocean/sea ice model with orthogonal curvilinear coordinates. *Ocean Modelling* **5**, 91-127 (2003).
59. T. Egorova *et al.*, Chemistry-climate model SOCOL: a validation of the present-day climatology. *Atmospheric Chemistry and Physics* **5**, 1557-1576 (2005).
60. M. Schraner *et al.*, Chemistry-climate model SOCOL: version 2.0 with improved transport and chemistry/microphysics schemes. *Atmospheric Chemistry and Physics* **8**, 5957-5974 (2008).

61. M. Calisto, I. Usoskin, E. Rozanov, T. Peter, Influence of galactic cosmic rays on atmospheric composition and dynamics. *Atmospheric Chemistry and Physics* **11**, 4547-4556 (2011).
62. I. G. Usoskin, G. A. Kovaltsov, Cosmic ray induced ionization in the atmosphere: Full modeling and practical applications. *Journal of Geophysical Research: Atmospheres* **111**, (2006).
63. I. G. Usoskin, G. A. Kovaltsov, I. A. Mironova, Cosmic ray induced ionization model CRAC:CRII: An extension to the upper atmosphere. *Journal of Geophysical Research: Atmospheres* **115**, (2010).
64. H. Porter, C. Jackman, A. Green, Efficiencies for production of atomic nitrogen and oxygen by relativistic proton impact in air. *The Journal of Chemical Physics* **65**, 154-167 (1976).
65. S. Solomon, D. Rusch, J.-C. Gérard, G. Reid, P. Crutzen, The effect of particle precipitation events on the neutral and ion chemistry of the middle atmosphere: II. Odd hydrogen. *Planetary and Space Science* **29**, 885-893 (1981).
66. J. Kirkby *et al.*, Role of sulphuric acid, ammonia and galactic cosmic rays in atmospheric aerosol nucleation. *Nature* **476**, 429-433 (2011).
67. S. Muthers *et al.*, The coupled atmosphere–chemistry–ocean model SOCOL-MPIOM. *Geosci. Model Dev.* **7**, 2157-2179 (2014).
68. PAGES2k Consortium *et al.*, A global multiproxy database for temperature reconstructions of the Common Era. *Scientific Data* **4**, 170088 (2017).
69. PAGES 2k Consortium, Continental-scale temperature variability during the past two millennia. *Nature Geosci* **6**, 339-346 (2013).
70. G. A. Meehl, J. M. Arblaster, K. Matthes, F. Sassi, H. van Loon, Amplifying the Pacific climate system response to a small 11-year solar cycle forcing. *Science* **325**, 1114-1118 (2009).
71. R. Checa-Garcia, M. I. Hegglin, D. Kinnison, D. A. Plummer, K. P. Shine, Historical tropospheric and stratospheric ozone radiative forcing using the CMIP6 database. *GRL* **45**, 3264-3273 (2018).
72. K. B. Tokarska *et al.*, Past warming trend constrains future warming in CMIP6 models. *Science Advances* **6**, eaaz9549 (2020).

73. I. Suter, R. Zech, J. Anet, T. Peter, Impact of geomagnetic excursions on atmospheric chemistry and dynamics. *Clim Past* **10**, 1183-1194 (2014).
74. N. Butchart, The Brewer-Dobson circulation. *Reviews of Geophysics* **52**, 157-184 (2014).
75. Y. Kuroda, K. Yamazaki, K. Shibata, Role of ozone in the solar cycle modulation of the North Atlantic Oscillation. *Journal of Geophysical Research: Atmospheres* **113**, (2008).
76. K. Kodera, Solar cycle modulation of the North Atlantic Oscillation: Implication in the spatial structure of the NAO. *GRL* **29**, 59-51-59-54 (2002).
77. A. S. Dalton *et al.*, Was the Laurentide Ice Sheet significantly reduced during marine isotope stage 3? *Geology* **47**, 111-114 (2019).
78. A. S. Dalton, S. A. Finkelstein, P. J. Barnett, S. L. Forman, Constraining the Late Pleistocene history of the Laurentide Ice Sheet by dating the Missinaibi Formation, Hudson Bay Lowlands, Canada. *Quaternary Science Reviews* **146**, 288-299 (2016).
79. A. E. Carlson, L. Tarasov, T. Pico, Rapid Laurentide ice-sheet advance towards southern last glacial maximum limit during marine isotope stage 3. *Quaternary Science Reviews* **196**, 118-123 (2018).
80. S. O. Rasmussen *et al.*, A stratigraphic framework for abrupt climatic changes during the Last Glacial period based on three synchronized Greenland ice-core records: refining and extending the INTIMATE event stratigraphy. *Quaternary Science Reviews* **106**, 14-28 (2014).
81. G. Deplazes *et al.*, Links between tropical rainfall and North Atlantic climate during the last glacial period. *Nature Geoscience* **6**, 213-217 (2013).
82. WAIS Divide Project Members, Precise inter-polar phasing of abrupt climate change during the last ice age. *Nature* **520**, 661-665 (2015).
83. J. Stevenson, G. Hope, A comparison of late Quaternary forest changes in New Caledonia and northeastern Australia. *Quatern Res* **64**, 372-383 (2005).
84. A. Cooper *et al.*, Abrupt warming events drove Late Pleistocene Holarctic megafaunal turnover. *Science* **349**, 602-606 (2015).
85. L. Becerra-Valdivia, T. Higham, The timing and effect of the earliest human arrivals in North America. *Nature* **584**, 93-97 (2020).

86. J. Hansford *et al.*, Early Holocene human presence in Madagascar evidenced by exploitation of avian megafauna. *Science Advances* **4**, doi: 10.1126/sciadv.aat6925 (2018).
87. J. F. O'Connell *et al.*, When did *Homo sapiens* first reach Southeast Asia and Sahul? *PNAS* **115**, 8482-8490 (2018).
88. R. Tobler *et al.*, Aboriginal mitogenomes reveal 50,000 years of regionalism in Australia. *Nature* **544**, 180-184 (2017).
89. F. Saltre *et al.*, Climate change not to blame for late Quaternary megafauna extinctions in Australia. *Nat Commun* **7**, doi: 10.1038/ncomms10511 (2016).
90. F. Saltr e *et al.*, Climate-human interaction associated with southeast Australian megafauna extinction patterns. *Nature Comms* **10**, 5311 (2019).
91. S. Rule *et al.*, The aftermath of megafaunal extinction: Ecosystem transformation in Pleistocene Australia. *Science* **335**, 1483-1486 (2012).
92. L. C. White, K. J. Mitchell, J. J. Austin, Ancient mitochondrial genomes reveal the demographic history and phylogeography of the extinct, enigmatic thylacine (*Thylacinus cynocephalus*). *Journal of biogeography* **45**, 1-13 (2018).
93. M. Staubwasser *et al.*, Impact of climate change on the transition of Neanderthals to modern humans in Europe. *Proceedings of the National Academy of Sciences* **115**, 9116-9121 (2018).
94. T. Higham *et al.*, The earliest evidence for anatomically modern humans in northwestern Europe. *Nature* **479**, 521-524 (2011).
95. J.-J. Hublin *et al.*, Initial Upper Palaeolithic *Homo sapiens* from Bacho Kiro Cave, Bulgaria. *Nature* **581**, 299-302 (2020).
96. T. Higham *et al.*, The timing and spatiotemporal patterning of Neanderthal disappearance. *Nature* **512**, 306-309 (2014).
97. C. Lalueza-Fox *et al.*, A Melanocortin 1 receptor allele suggests varying pigmentation among Neanderthals. *Science* **318**, 1453-1455 (2007).
98. J. I. Svendsen *et al.*, Geo-archaeological investigations of Palaeolithic sites along the Ural Mountains e On the northern presence of humans during the last Ice Age. *Quatern Sci Rev* **29**, 3138-3156 (2010).

99. J. M. Bowler *et al.*, New ages for human occupation and climatic change at Lake Mungo, Australia. *Nature* **421**, 837-840 (2003).
100. S. O'Connor, R. Ono, C. Clarkson, Pelagic fishing at 42,000 years before the present and the maritime skills of modern Humans. *Science* **334**, 1117-1121 (2011).
101. M. C. Langley, S. O'Connor, 3 Exploring red ochre use in Timor-Leste and surrounds: Headhunting, burials, and beads. *The Archaeology of Portable Art: Southeast Asian, Pacific, and Australian Perspectives*, 25-36 (2018).
102. J. T. Faith, Taphonomic and paleoecological change in the large mammal sequence from Boomplaas Cave, western Cape, South Africa. *Journal of Human Evolution* **65**, 715-730 (2013).
103. B. M. Chase, M. Chevalier, A. Boom, A. S. Carr, The dynamic relationship between temperate and tropical circulation systems across South Africa since the last glacial maximum. *Quaternary Science Reviews* **174**, 54-62 (2017).
104. H. J. Deacon, Excavations at Boomplaas cave - a sequence through the Upper Pleistocene and Holocene in South Africa. *World Archaeology* **10**, 241-257 (1979).
105. J. T. Faith, Taphonomic and paleoecological change in the large mammal sequence from Boomplaas Cave, Western Cape, South Africa. *Journal of Human Evolution* **65**, 715-730 (2013).
106. J. Pargeter, E. Loftus, A. Mackay, P. Mitchell, B. Stewart, New ages from Boomplaas Cave, South Africa, provide increased resolution on late/terminal Pleistocene human behavioral variability. *Azania: Archaeological Research in Africa* **53**, 156-184 (2018).
107. J. T. Faith, R. L. Lyman, *Paleozoology and Paleoenvironments: Fundamentals, Assumptions, Techniques*. (Cambridge University Press, Cambridge, 2019).
108. J. Sealy, J. Lee-Thorp, E. Loftus, J. T. Faith, C. W. Marean, Late Quaternary environmental change in the Southern Cape, South Africa, from stable carbon and oxygen isotopes in faunal tooth enamel from Boomplaas Cave. *Journal of Quaternary Science* **31**, 919-927 (2016).
109. A. S. Talma, J. C. Vogel, Late Quaternary palaeotemperatures derived from a speleothem from Cango Caves, Cape Province, South Africa. *Quaternary Research* **37**, 203-213 (1992).

110. B. M. Chase, A. Boom, A. S. Carr, M. E. Meadows, P. J. Reimer, Holocene climate change in southernmost South Africa: rock hyrax middens record shifts in the southern westerlies. *Quaternary Science Reviews* **82**, 199-205 (2013).
111. M. Aubert *et al.*, Palaeolithic cave art in Borneo. *Nature* **564**, 254-257 (2018).
112. M. Aubert *et al.*, Pleistocene cave art from Sulawesi, Indonesia. *Nature* **514**, 223-227 (2014).
113. R. F. Rifkin *et al.*, Evaluating the photoprotective effects of ochre on human skin by in vivo SPF assessment: implications for human evolution, adaptation and dispersal. *PLoS One* **10**, e0136090 (2015).
114. A. W. Pike *et al.*, U-series dating of Paleolithic art in 11 caves in Spain. *Science* **336**, 1409-1413 (2012).
115. A. G. Hogg *et al.*, SHCal13 Southern Hemisphere calibration, 0–50,000 years cal BP. *Radiocarbon* **55**, 1889-1903 (2013).
116. A. Svensson *et al.*, A 60 000 year Greenland stratigraphic ice core chronology. *Clim Past* **4**, 47-57 (2008).
117. D. E. Nelson, G. Chaloupka, C. Chippindale, M. S. Alderson, J. R. Southon, Radiocarbon dates for beeswax figures in the prehistoric rock art of northern Australia. *Archaeometry* **37**, 151-156 (1995).
118. S. O'Connor, B. L. Fankhauser, in *Histories of old ages: essays in honour of Rhys Jones*. (Pandanus Books, 2001).
119. N. J. Conard, A female figurine from the basal Aurignacian of Hohle Fels Cave in southwestern Germany. *Nature* **459**, 248 (2009).
120. R. Vogelsang, *Middle-Stone-Age-Fundstellen in Südwest-Namibia*. (Heinrich-Barth-Institut, 1998), vol. 11.
121. J. Clottes *et al.*, Un art très ancien en Roumanie. Les dates de Coliboaia. (2011).
122. H. Floss, N. Rouquerol, in *Éditions Musée-forum Aurignac, Aurignac*. (2007).
123. H. Valladas, Direct radiocarbon dating of prehistoric cave paintings by accelerator mass spectrometry. *Meas Sci Technol* **14**, 1487-1492 (2003).
124. T. Jones *et al.*, Radiocarbon age constraints for a Pleistocene–Holocene transition rock art style: the Northern Running Figures of the East Alligator River region, western Arnhem Land, Australia. *Journal of Archaeological Science: Reports* **11**, 80-89 (2017).

125. J. Ross, K. Westaway, M. Travers, M. J. Morwood, J. Hayward, Into the Past: A Step Towards a Robust Kimberley Rock Art Chronology. *Plos One* **11**, (2016).
126. P. S. Tacon, T. Huisheng, M. Aubert, Naturalistic animals and hand stencils in the rock art of Xinjiang Uyghur Autonomous Region, northwest China. *Rock Art Research: The Journal of the Australian Rock Art Research Association (AURA)* **33**, 19 (2016).
127. S. di Lernia *et al.*, Inside the "African Cattle Complex": Animal Burials in the Holocene Central Sahara. *Plos One* **8**, (2013).
128. B. David *et al.*, A 28,000 year old excavated painted rock from Nawarla Gabarnmang, northern Australia. *Journal of Archaeological Science* **40**, 2493-2501 (2013).
129. L. G. Straus, M. R. G. Morales, The Magdalenian settlement of the Cantabrian region (Northern Spain): The view from El Miron Cave. *Quaternary International* **272**, 111-124 (2012).
130. W. A. Neves, A. G. M. Araujo, D. V. Bernardo, R. Kipnis, J. K. Feathers, Rock Art at the Pleistocene/Holocene Boundary in Eastern South America. *Plos One* **7**, (2012).
131. E. Malotki, H. D. Wallace, Columbian mammoth petroglyphs from the San Juan River near Bluff, Utah, United States. *Rock Art Research: The Journal of the Australian Rock Art Research Association (AURA)* **28**, 143 (2011).
132. D. Huyge *et al.*, First evidence of Pleistocene rock art in North Africa: securing the age of the Qurta petroglyphs (Egypt) through OSL dating. *Antiquity* **85**, 1184-1193 (2011).
133. S. O'Connor, K. Aplin, E. St Pierre, Y.-x. Feng, Faces of the ancestors revealed: discovery and dating of a Pleistocene-age petroglyph in Lene Hara Cave, East Timor. *Antiquity* **84**, 649-665 (2010).
134. M. Smith, A. Watchman, J. Ross, Direct dating indicates a Mid-Holocene age for archaic rock engravings in arid Central Australia. *Geoarchaeology: An International Journal* **24**, 191-203 (2009).
135. M. Dietzel, H. Kolmer, P. Pölt, S. Simic, Desert varnish and petroglyphs on sandstone—geochemical composition and climate changes from Pleistocene to Holocene (Libya). *Chemie der Erde-Geochemistry* **68**, 31-43 (2008).
136. A. W. Pike *et al.*, Verification of the age of the Palaeolithic cave art at Creswell Crags, UK. *Journal of Archaeological Science* **32**, 1649-1655 (2005).

137. N. Cole, A. Watchman, AMS dating of rock art in the Laura Region, Cape York Peninsula, Australia—protocols and results of recent research. *Antiquity* **79**, 661-678 (2005).
138. V. Plagnes *et al.*, Cross dating (Th/U-14 C) of calcite covering prehistoric paintings in Borneo. *Quaternary Research* **60**, 172-179 (2003).
139. R. G. Bednarik, About the age of Pilbara rock art. *Anthropos*, 201-215 (2002).
140. K. Steelman, M. Rowe, V. Shirokov, J. Southon, Radiocarbon dates for pictographs in Ignatievskaya Cave, Russia: Holocene age for supposed Pleistocene fauna. *Antiquity* **76**, 341-348 (2002).
141. D. S. Whitley, R. I. Dorn, Rock art chronology in eastern California. *World Archaeology* **19**, 150-164 (1987).
142. D. L. Hoffmann *et al.*, U-Th dating of carbonate crusts reveals Neandertal origin of Iberian cave art. *Science* **359**, 912-915 (2018).
143. M. Aubert *et al.*, Palaeolithic cave art in Borneo. *Nature* **564**, 254 (2018).
144. M. Aubert *et al.*, Earliest hunting scene in prehistoric art. *Nature* **576**, 442-445 (2019).